Materials and Solidification

Research Article

Multi-scale simulation of thermal processes and microstructure evolution in wire arc additive manufacturing of 921A steel

Lei Shi[1,✉], Xiaohui Lyu[1], Ji Chen[1], Chuansong Wu[1], Ashish Kumar[1], Ming Zhai[2], Wenjian Ren[3]

Cite this article: Shi L, Lyu X, Chen J, et al. *Materials and Solidification* 2025, **1**(1): 9580003. https://doi.org/10.26599/MAS.2025.9580003

ABSTRACT: Wire arc additive manufacturing (WAAM) offers distinct advantages, including low equipment cost, high deposition efficiency, and suitability for fabricating large-scale components. 921A steel (10CrNi3MoV) is widely used in the offshore industry and shipbuilding, making the development of WAAM technology for 921A steel crucial for manufacturing and repairing ship components. In this study, a two-dimensional melting–solidification model was developed to investigate the melt pool dynamics and microstructure evolution during the WAAM process. This model integrates computational fluid dynamics (CFD) with the cellular automata (CA) method, utilizing the open-source ExaCA code for microstructural simulation. The model successfully predicted the temperature and flow fields, as well as the microstructural evolution within the deposition layer. Macroscopic metallography revealed columnar grains aligned with the heat flow direction, accompanied by acicular and granular ferrite, as well as bainitic morphologies. The simulated forming dimensions at various deposition speeds agreed reasonably well with the experimental results. An increased deposition speed reduced the fluid flow intensity within the molten pool. The ExaCA simulation demonstrated that columnar grains grew perpendicular to the fusion line, whereas nucleated equiaxed grains formed in the center of the molten pool under low-temperature gradients, obstructing the progression of the original columnar grains.

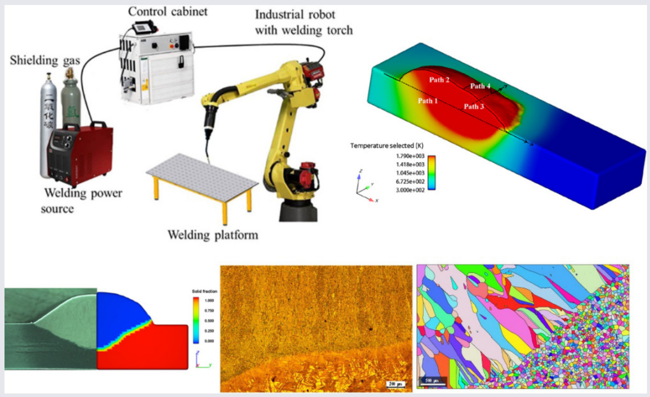

KEYWORDS: wire arc additive manufacturing (WAAM); 921A steel; microstructure; cellular automata (CA); deposition speed; columnar grains

1 Introduction

Additive manufacturing (AM) is recognized as a transformative technology driving the fourth industrial revolution and is characterized by the layer-by-layer addition of materials based on a digital model. This approach offers supreme design flexibility, rapid prototyping capabilities, and the potential for customized production, making it a critical tool in modern component manufacturing. This allows individual components to exhibit targeted characteristics, such as hardness, environmental adaptability, and corrosion resistance, precisely where they are most needed [1,2]. As one of the key AM methods, wire arc additive manufacturing (WAAM) is particularly well suited for producing complex, large-scale steel components because of its high efficiency, cost-effectiveness, adaptability to complex environments, and versatility. However, the microstructure and mechanical characteristics of parts fabricated through WAAM are critical considerations. During the WAAM process, the temperature of the deposited material repeatedly fluctuates as additional layers are added, significantly influencing the microstructure and resulting properties. These temperature fluctuations, referred to as thermal cycles, play a crucial role in determining the final performance of the manufactured part. Consequently, studying the effects of thermal cycles on the microstructure and mechanical characteristics is essential for optimizing processing parameters and enhancing material performance [3].

921A steel (10CrNi3MoV) is a domestically produced low-alloy, tempered high-strength steel in China, renowned for its excellent combination of mechanical properties, toughness, weldability, and corrosion resistance. These characteristics make it a preferred material for manufacturing critical components in ocean engineering, particularly in shipbuilding. Traditionally, manual arc welding has been the primary method for joining this steel. However, this technique is associated with limited efficiency,

[1] MOE Key Lab for Liquid–Solid Structure Evolution and Materials Processing, Institute of Materials Joining, Shandong University, Jinan 250061, China. [2] Metals and Chemistry Research Institute, China Academy of Railway Sciences Co., Ltd., Beijing 100081, China. [3] Shandong Aotai Electric Co., Ltd., Jinan 250101, China.

✉ Corresponding author. E-mail: lei.shi@sdu.edu.cn

Received: November 28, 2024; Revised: December 26, 2024; Accepted: January 17, 2025

high physical demands on workers, and difficult operating environments. With advancements in automation technology, gas-shielded welding has emerged as a viable alternative, significantly enhancing welding efficiency, reducing labor intensity, and improving overall operational effectiveness [4,5]. WAAM offers high manufacturing efficiency and cost-effectiveness, making it particularly advantageous for producing massive metallic structures. It is well-suited for the cost-efficient, high-productivity near-net shaping of intricate, large-scale parts and has extensive applications in biomedical, aerospace, marine, and automotive industries. Consequently, WAAM technology holds significant potential for the production and repair of critical ship components fabricated from 921A steel.

Tian *et al.* [6] utilized cold metal transfer (CMT) technology to perform multilayer single-pass tests on 921A steel, focusing on the analysis of its mechanical properties. While these experimental results contribute to the optimization of process parameters, they fail to fully elucidate the underlying mechanisms of additive layer formation. To gain deeper insights into the metal deposition process, an increasing number of researchers are employing numerical simulation techniques to study macroscopic heat and mass transfer behaviors. For example, Ou *et al.* [7] simulated the single-pass deposition process of H13 tool steel, highlighting the importance of cooling rate and G/R solidification parameters for predicting the WAAM solidification microstructure. Similarly, Cadiou *et al.* [8] established a three-dimensional (3D) model incorporating complete coupling between the welding wire and the molten pool, effectively capturing the complex dynamics of droplet transition in CMT-AM. Ji *et al.* [9] applied a CFD model to investigate the effects of ultrasonic vibrations on WAAM, revealing that acoustic streaming enhanced heat transfer, increased the deposition layer width, and reduced its height and depth.

WAAM typically operates with heat inputs ranging from 10 to 100 J/mm, where the heat dissipates primarily through conduction into the substrates and components, forced convection via the shielding gas, and radiation to the atmosphere. However, as the number of deposited layers increases, heat dissipation through conduction becomes less effective. The large substrate area facilitates cooling of the initially deposited layers, reducing heat accumulation in subsequent layers [10]. The WAAM process is inherently a multi-scale and multi-physics coupling process, encompassing macroscopic phenomena such as heat and mass transfer and microscopic mechanisms such as grain growth kinetics within the melt pool. The interplay between grain growth and recrystallization strongly influences the final microstructure and mechanical properties, as they depend on the unique thermal history experienced during manufacturing [11]. Utilizing microstructure simulation technology is crucial for understanding the complex dynamics of the additive process. This knowledge is key to ensuring uniform internal grain structures and achieving superior mechanical properties in the fabricated components [12,13].

Microstructure simulation methods primarily include Monte Carlo (MC) [14,15], phase field (PF) [16,17], and cellular automata (CA) [18–20] methods. Among these methods, the CA method, which combines a probabilistic approach with the physical mechanisms of grain nucleation and growth, is widely utilized for microstructure simulations. This method offers accurate predictions of material microstructures and effectively replicates experimentally observed grain size distributions and textures [21,22].

For example, Zinoviev *et al.* [23] employed the CA method to model two-dimensional grain growth and texture evolution in 316L stainless steel fabricated by selective laser melting (SLM), achieving results in good qualitative agreement with experimental observations. Gu *et al.* [24] simulated the solidification of a GTAW molten pool in a binary alloy (Al–Cu), demonstrating that higher cooling rates lead to finer primary dendritic trunks and formation of secondary and tertiary dendritic arms. The Mines Paris Tech team [25,26] modelled the evolution of grain structures in GTAW-processed URANUS 2202 duplex stainless steel and 316L stainless steel. Their work on URANUS 2202 introduced parallel computing and a dynamic allocation strategy for CA meshes to reduce computational costs, while their study on 316L validated the model's accuracy through comparisons with electron back scattered diffraction (EBSD) results. Koepf *et al.* [21,27] combined analytical solutions and finite element (FE) methods to derive macroscopic thermal histories and generated microstructure simulations of SEBM solidification, which were consistent with experimental data. Rolchigo *et al.* [28,29] from Oak Ridge National Laboratory developed the open-source ExaCA model, integrating macroscopic temperature field data from OpenFOAM to simulate the solidification microstructure of laser-based powder bed fusion (LPBF) processes. The CA model used in this work is primarily based on the ExaCA program developed by their team.

To address the identified research gaps, this study comprehensively investigated the single-pass single-layer deposition process for 921A steel in WAAM. This work combines experimental analysis, FLOW-3D temperature field modeling, and multi-scale microstructure simulation using the CA method. The dimensions and material flow of the deposition layer are examined at various deposition speeds, and the structure of the grains in the cross-section of the molten pool is simulated. The primary objective is to analyze the microstructural characteristics of WAAM systematically and elucidate the effects of process parameters on the resulting microstructure of 921A steel. This research aims to provide a theoretical foundation for optimizing the manufacturing and repair processes of critical ship components.

2 Materials and methods

The experimental substrate used in this study was a 921A steel plate (grade 10CrNi3MoV) with dimensions of 250 mm × 50 mm × 5 mm. The feedstock material comprised a WM960S gas-shielded welding electrode with a diameter of 1.2 mm. Single-pass single-layer depositions were fabricated using a gas metal arc welding (GMAW)-based AM process. The schematic representation of the experimental setup for the GMAW-based AM system is depicted in Fig. 1.

The shielding gas used in the experiment was a mixture of 80% Ar and 20% CO_2 with a gas flow rate of 20 L/min. The distance between the top surface and the nozzle of the substrate was kept constant as 15 mm. The deposition current was 210 A, the deposition voltage 26.3 V, and the wire feed speed 5.9 m/min. Four sets of deposition speeds, ranging 3–6 mm/s, were selected for the additive samples.

3 Numerical model setup

3.1 Macroscopic CFD model

The macroscopic model is established using FLOW-3D software, which employs the TruVOF method to accurately track the free surface of the molten pool, making it particularly well-suited for additive manufacturing simulations. The model incorporates the

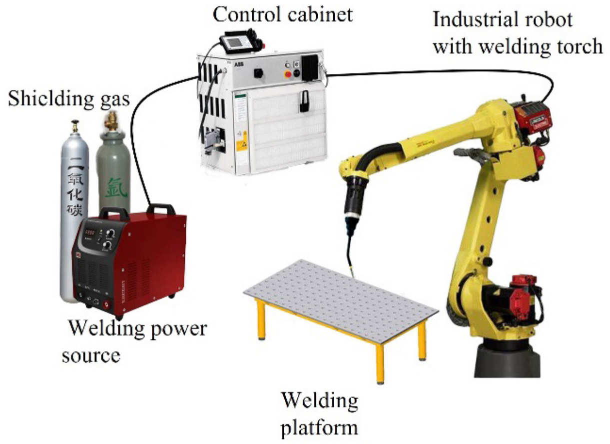

Fig. 1 Experimental system of GMAW-based additive manufacturing.

following simplifying assumptions: (1) the substrate is modeled as an incompressible Newtonian fluid, and the flow within the melt pool is assumed to be laminar; (2) the molten droplets are assumed to possess identical physical properties to those of the substrate material; (3) the influence of the shielding gas on the melt pool dynamics is disregarded.

The mass continuity, energy, and momentum equations used in the calculation process are as Eqs. (1)–(3):

$$\nabla \cdot V = \frac{\dot{m}}{\rho} \tag{1}$$

$$\frac{\partial h}{\partial t} + V \cdot \nabla h = \frac{1}{\rho}\nabla \cdot (k\nabla T) + h_s \tag{2}$$

$$\frac{\partial V}{\partial t} + V \cdot (\nabla V) = -\frac{1}{\rho}\nabla P + \mu \nabla^2 V + S_M \tag{3}$$

where V is the velocity vector; $\dot{m}$ is the mass source term associated with the formation of the droplet; ρ is the density; h is the enthalpy; k is the thermal conductivity; T is the temperature; h_s is the enthalpy source phase related to the mass source term; P is the pressure; μ is the kinetic viscosity coefficient; S_M is the momentum source term.

For the GMAW-based AM process, the heat input mainly consists of the arc heat and the enthalpy of the molten droplet. The enthalpy of the molten droplet is not treated as a separate heat source in the model, but the heat of the molten droplet is considered together in the arc heat source. Therefore, a double-ellipsoid heat source is used to characterize the arc heat flow distribution, and its distribution functions are as Eqs. (4) and (5) [30]:

$$q(x,y) = \frac{6\sqrt{3} f_f \eta IU}{a_f bc\pi\sqrt{\pi}} \exp\left(-\frac{3x^2}{a_f^2} - \frac{3y^2}{b^2} - \frac{3z^2}{c^2}\right) (x > 0) \tag{4}$$

$$q(x,y) = \frac{6\sqrt{3} f_r \eta IU}{a_r bc\pi\sqrt{\pi}} \exp\left(-\frac{3x^2}{a_r^2} - \frac{3y^2}{b^2} - \frac{3z^2}{c^2}\right) (x < 0) \tag{5}$$

where a_f and a_r represent the front and back halves of the arc heat source, respectively; a_f, a_r, b, and c are the heat source distribution parameters; f_f and f_r are the shares of the arc heat input to the front and back halves of the ellipsoid, respectively; $f_f + f_r = 2$. The double-ellipsoid heat source is applied to the surface of the molten pool, which moves along the deposition direction at the specified deposition speed.

The process of molten droplet formation and detachment from the wire is omitted, with the droplets assumed to be spherical. Under the influence of electromagnetic forces and gravity, the molten droplets are modeled as entering the molten pool vertically downward at a defined velocity, aligned with the centerline of the deposited layer. The droplet temperature is set to 2100 K, with a radius of 0.7 mm and a transition frequency of 125 droplets per second at a velocity of 0.97 m/s. Furthermore, the model incorporates the effects of gravity, buoyancy, electromagnetic forces, and arc pressure on the molten pool fluid dynamics [31].

As illustrated in Fig. 2, the model utilizes a half-domain computational approach. The domain is classified into two regions: air and substrate. The X-axis represents the direction of heat source movement; the Y-axis corresponds to the width of the substrate; the Z-axis denotes the growth direction of the deposited layer. The model is symmetric about the ZOX plane and encompasses dimensions of 35 mm × 10 mm × 10 mm. Within this domain, the substrate has a thickness of 5 mm, while the air layer extends to a height of 5 mm.

In the model, the ZOX plane is designated as the symmetry boundary (S), the top surface of the computational domain as the pressure boundary (P), the bottom surface as the wall boundary (W), and the remaining three planes as continuous boundaries (C). During the deposition process, the substrate remains stationary while the arc heat source moves in the positive X-axis direction. A mesh with a size of 0.25 mm is applied, and the generalized minimum residual method (GMRES) solver is employed to resolve the coupled pressure–velocity equations. The sharp interface is tracked using the Split Lagrangian method. The initial time step is set at 1×10^{-5} s, with a total simulation time of 4.0 s. The model adopts the same deposition parameters as those used in the experiments, and the thermophysical behaviors of the materials are detailed in Table 1.

3.2 Microscopic CA model

The CA method operates by dividing the simulation domain into a grid of regular computational cells, each associated with specific state variables. When a time- and space-dependent temperature field is applied, the state of each cell is updated at each time step based on the thermal input. To simulate the solidification process, macroscopic thermal history data must be integrated into the CA model. This approach enables the prediction of the evolution of the solidification microstructure during WAAM. However, because the grain-scale CA method does not account for fine-scale details of solidification within grains, such as dendritic arm spacing development or solute partitioning at dendrite tips, it is particularly suitable for modeling solidification across a wide range of thermal conditions [29].

The simulation region initially consists of all solid cells. The

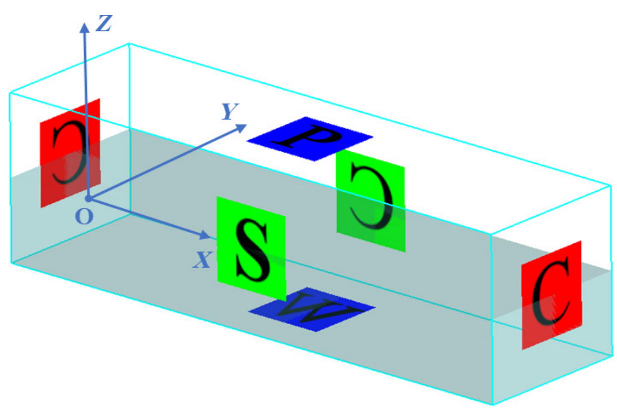

Fig. 2 Boundary diagram of numerical calculation model.

Table 1 Thermophysical characteristics of 921A steel and related parameters

Parameter	Value
Density	$7850\ \mathrm{kg/m^3}$
Liquidus temperature	1790 K
Solidus temperature	1760 K
Vapour temperature	2900 K [32]
Latent heat of fusion	$2.5\times10^5\ \mathrm{J/kg}$
Thermal conductivity	$25.4\ \mathrm{W/(m\cdot K)}$
Coefficient of thermal expansion	$2.5\times10^{-5}\ \mathrm{K^{-1}}$
Specific heat	Temperature-dependent [33]
Viscosity	$0.006\ \mathrm{kg/(m\cdot s)}$
Temperature coefficient of surface tension	$-0.0003\ \mathrm{N/(m\cdot K)}$ [34]
Surface tension	1.2 N/m [34]
Convective heat transfer coefficient	$25\ \mathrm{W/(m^2\cdot K)}$ [35]
Radiation emissivity	0.8 [35]
Magnetic permeability	$1.26\times10^{-6}\ \mathrm{H/m}$
Stefan–Boltzmann constant	$5.67\times10^{-8}\ \mathrm{W/(m^2\cdot K^4)}$

cells with a melt-solidification process input from the macroscopic model are initialized as liquid, while all other cells remain in the solid state. The solid cells adjacent to the liquid cells become active and are assigned octahedra.

The grain growth depends on the velocity law of the dendrite tip. According to the decentered octahedron algorithm of the ExaCA model, the semi-diagonal direction of the active cell octahedra is consistent with the preferred <001> growth direction of dendrite solidification [36]. The growth rate of a given octahedral envelope is as Eq. (6):

$$\Delta L=\frac{\Delta t}{\Delta x}\left(A(\Delta T)^3+B(\Delta T)^2+C(\Delta T)\right) \tag{6}$$

where ΔL is the increment dimensionless size of the semi-diagonal L of the octahedron at each time step; Δt is the time step; Δx is the cell size; ΔT is the local undercooling value; the polynomial is the interfacial response function [37]; A, B, and C are the constants of the interfacial response function of the material.

For the growth of an active cell, the cell is considered “captured” when its diagonal length reaches a certain value that will engulf the center of the adjacent liquid cell. Cellular capture events include changing the state of the new cell to the active cell, assigning the grain identity (ID) of the old cell to the new cell, and assigning the initial size (L) to the octahedron of the newly activated cell. An active cell transitions to a solid state when it no longer has liquid cell neighbors, and its octahedral growth ceases to be monitored.

In addition to grain growth, heterogeneous nucleation is another major step in the CA method. During initialization, a random number between 0 and 1 is generated for each liquid cell (Eq. (7)):

$$P=N_0(\Delta x)^3 \tag{7}$$

where N_0 is the largest nucleation density. If this random number is less than the probability value, the cell is initialized as a “potential nucleus” cell. For each possible nucleation site, a critical supercooling ΔT_c is specified, and the value of ΔT_c follows a Gaussian distribution determined by ΔT_N and ΔT_σ, where ΔT_N is the mean nucleation undercooling value and ΔT_σ is the standard deviation [38]. When the subcooling at the nucleation site is lower than the critical subcooling and the cell is not captured by other grains, the nucleation is successful [39]. Formerly, the cell state changes from liquid to active, and the new grain ID value and the corresponding octahedron are assigned.

In the ExaCA model, the cell size, time step, nucleation parameters, substrate grain size (S_0), input and output file paths, and names are set in the top-level input file. The material input files, including the interface response function parameters, and solidification range and grain orientation files, are set. The input parameters used in the model are shown in Table 2.

3.3 Coupling scheme

Owing to the larger melt pool size and time step used in the CFD method than in the CA method, a unidirectional coupling scheme is employed in this study. Specifically, solidification data obtained from the CFD simulation are interpolated in both space and time using a linear interpolation method and then fed into the CA method to model the evolution of the grain structure. The solidification data for each cell include the X, Y, and Z spatial coordinates, the start and end time of solidification, and the cooling rate. The cooling rate, which is calculated from the macroscopic temperature field, ranges from 4 to 420 K/s, with the results falling within a reasonable range.

4 Results and discussion

4.1 Experimental characterization results

The results of single-layer single-pass experiments conducted at varying deposition speeds are presented in Table 3. The macroscopic metallographic analysis of the deposited layer reveals distinct columnar grains aligned with the direction of heat flow. A detailed examination of the microstructure in different regions of the joint for case 2 was performed (Fig. 3). For 921A steel, which is classified as a low-carbon, low-alloy material, the phase transformation behavior is influenced primarily by the chemical composition and cooling conditions of the weld metal [10].

During the deposition process, different regions experience varying numbers of thermal cycles, resulting in the development of unique microstructures. Figure 3(a) depicts the metallographic images of the base material, 921A steel, which consists of ferrite (F) and coarse pearlite (P), exhibiting a ribbon-like distribution. As shown in Fig. 3(b), the microstructure undergoes austenitization followed by rapid cooling, which leads to significant grain refinement and development of a fine, uniform martensite (M) structure. As shown in Fig. 3(c), the heat-affected zone (HAZ) contains coarse martensite due to prolonged exposure to elevated temperatures. As shown in Fig. 3(d), the central region of the molten pool experiences longer high-

Table 2 Input parameter values in CA model

Parameter	Value
Δt	10 μs
Δx	5 μm
A	$7.325\times10^{-6}\ \mathrm{m/(s\cdot K^3)}$
B	$3.12\ \mathrm{m/(s\cdot K^2)}$
C	0
N_0	$5\times10^{12}\ \mathrm{m^{-3}}$
ΔT_N	5 K
ΔT_σ	0.5 K
S_0	25 μm

Table 3 Experimental results at different deposition speeds

Case	Deposition speed (mm/s)	Macroscopic morphology	Cross-sectional metallography
1	3		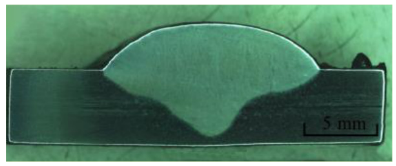
2	4		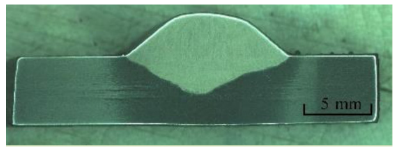
3	5	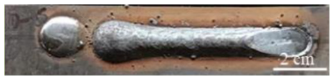	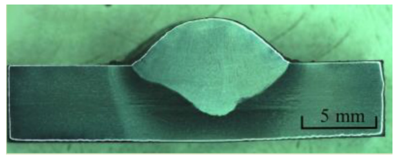
4	6		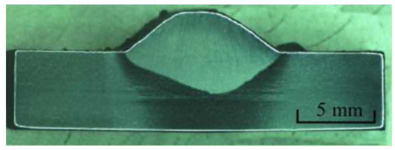

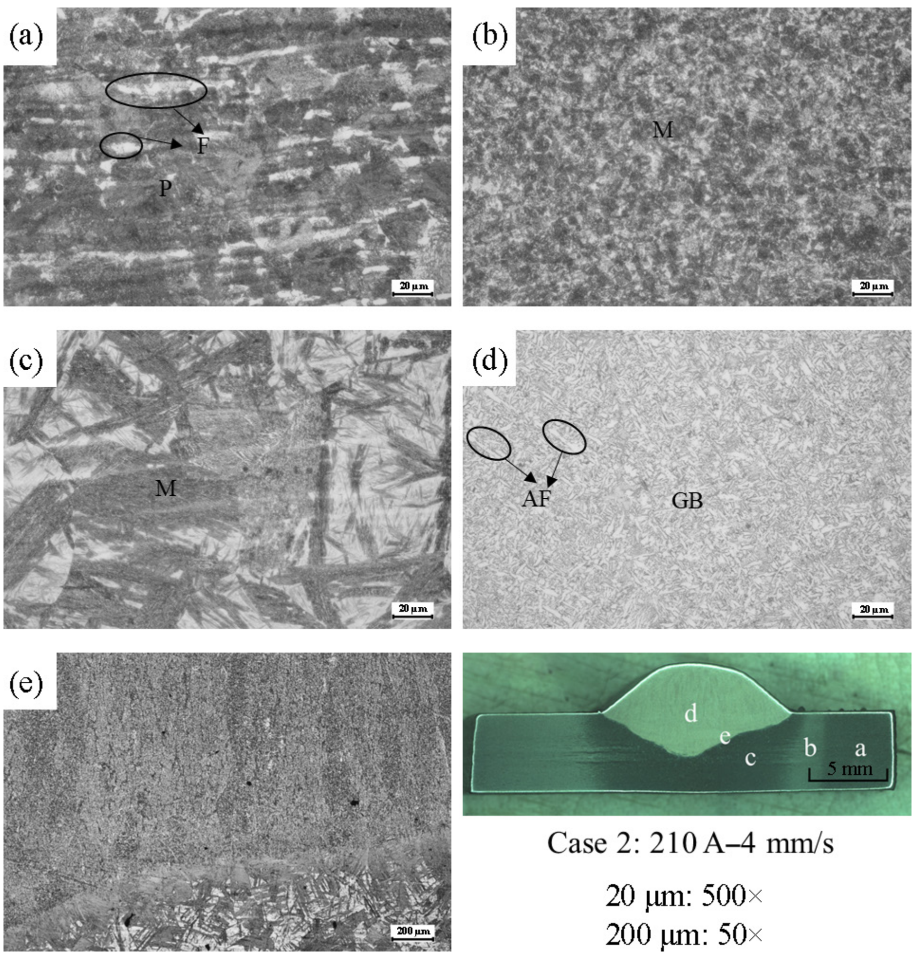

Fig. 3 Microstructural analysis at various locations for a deposition speed of 4 mm/s in case 2: (a) matrix structure; (b) fine-grained heat-affected zone (FG-HAZ); (c) coarse-grained heat-affected zone (CG-HAZ); (d) columnar crystal region; (e) fusion zone interface.

temperature residence time, leading to a smaller temperature gradient and a slower cooling rate, which results in a large constitution undercooling zone. This zone forms a columnar crystal structure consisting of granular bainite (GB) and acicular

清華大学出版社 Tsinghua University Press | SciOpen

ferrite (AF). Finally, the fusion line zone represents the uneven interface between the weld and substrate, where the metal above the fusion line grows toward the weld center, exhibiting columnar crystals (Fig. 3(e)).

4.2 Heat and mass flow behavior

Figure 4 presents both the experimental and simulation results of the molten pool cross-section at a deposition speed of 4 mm/s during the single-pass deposition process. The corresponding simulated and experimental geometric dimensions are displayed in Fig. 5. Notably, the deposition speed generally leads to a decreasing trend in both the width and height of the molten pool. Furthermore, the results from the simulation and experiments show strong agreement under identical deposition parameters, highlighting the reliability of the simulated model in predicting the molten pool behavior.

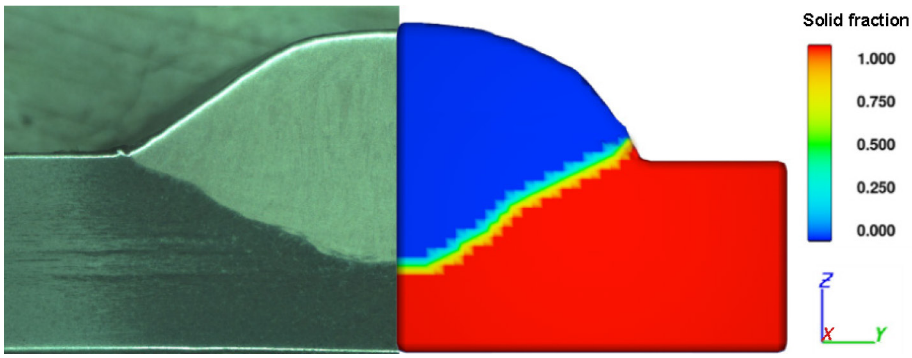

Fig. 4 Comparison of experimentally measured and simulated cross-sectional profiles at a deposition speed of 4 mm/s.

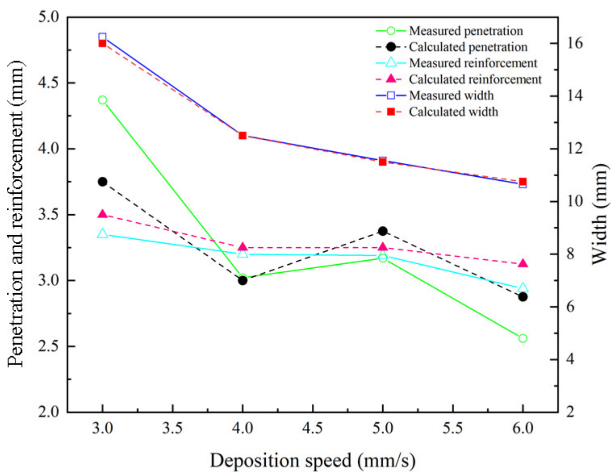

Fig. 5 Comparison of experimental and simulated forming dimensions.

To investigate the influence of the deposition speed on the molten pool flow dynamics, flow velocity profiles were extracted and plotted along both the free surface and just beneath the substrate (z = −0.0001 m) for paths 1–4, as illustrated in Fig. 6. The results presented in Fig. 7 reveal that the flow velocity along the free surface of the melt pool (paths 2 and 4) is generally greater than that within the melt pool (paths 1 and 3). For paths 1 and 3 inside the melt pool (Figs. 7(a) and 7(c)), the maximum flow velocity and its spatial extent occur at a deposition speed of 3 mm/s. As the deposition speed increases, both the flow velocity and its distribution within the melt pool decrease. In contrast, the flow velocity on the free surface of the melt pool fluctuates more along longitudinal path 2 and transverse path 4 (Figs. 7(b) and 7(d)). These fluctuations are attributed to the dynamic interplay of transient forces, such as surface tension and the Marangoni effect, at the free interface. Despite these variations, the overall peak flow rate on the free surface follows a trend similar to that observed within the melt pool. Collectively, both the internal and surface

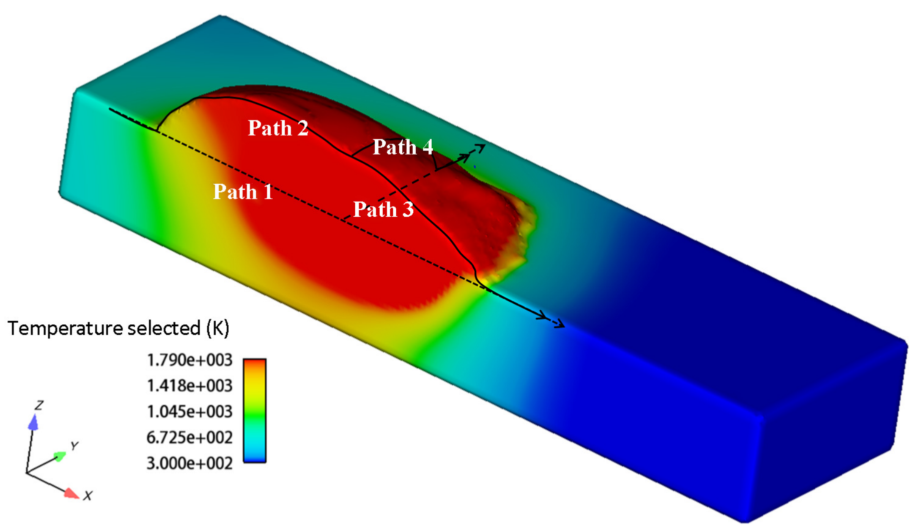

Fig. 6 Schematic diagram of flow velocity extraction path.

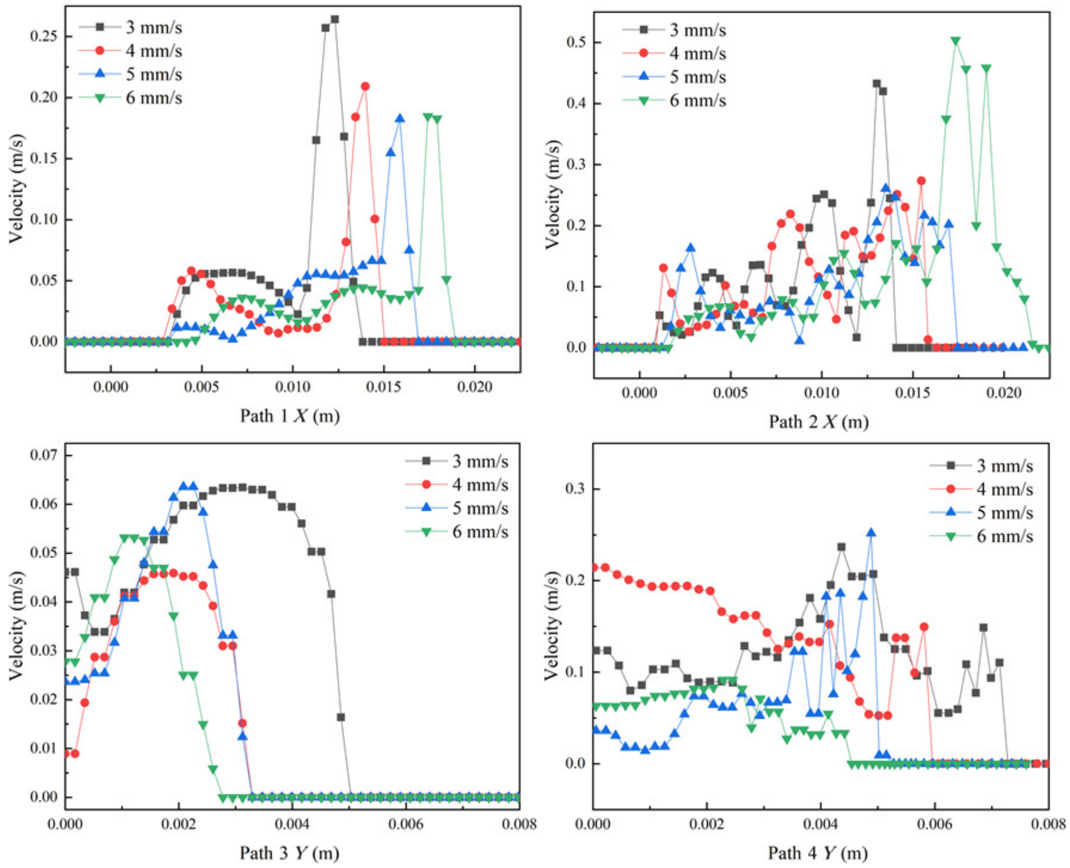

Fig. 7 Flow velocity profiles at free surface and within molten pool at various deposition speeds.

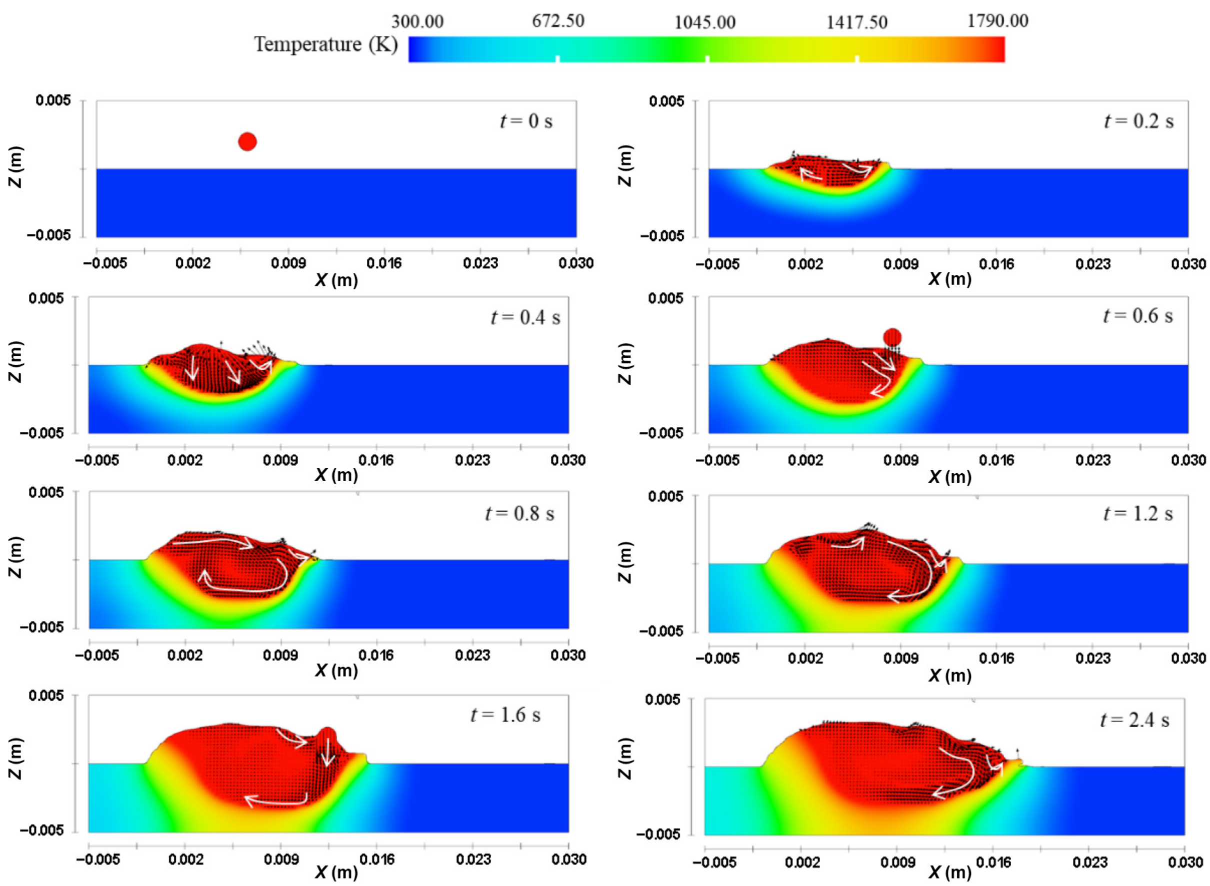

Fig. 8 Temperature and velocity distributions in longitudinal section of melt pool ($Y = 0$) at various time intervals.

flow characteristics indicate a reduction in the flow capability of the molten pool as the deposition speed increases.

Figure 8 presents an analysis of the temperature and flow fields in the longitudinal section ($Y = 0$) of the melt pool at various time intervals in the case 2. The highest temperature is observed at the center of the melt pool, gradually decreasing towards the tail and bottom, with a steeper temperature gradient observed at the front of the pool than at the rear. In the central region of the melt pool where the temperature gradient is most pronounced, the surface tension is minimized, and electromagnetic forces dominate. These forces, in conjunction with gravity and the impact of falling droplets, drive the molten metal to flow downward. In regions further from the center, the molten metal undergoes reflux motion along the bottom of the melt pool, circulating toward both the front and rear. In this area, surface tension plays a dominant role. Ultimately, the molten metal contracts inward and forms a bulging structure, resulting in the deposition of material at the tail of the melt pool.

Figure 9 illustrates the temperature and flow field distributions at different time intervals in the cross-sectional view of melt pool ($x = 0.008375$ m). Initially, the molten pool area expands due to the combined effects of the arc heat and droplet heat input. As cooling and solidification progress, the molten pool shrinks. The momentum imparted by the falling droplets is absorbed by the molten pool, driving the molten metal downward to the pool's bottom and subsequently toward the pool's sides. This flow behavior transports high-temperature liquid from the center of the melt pool to the surrounding regions while also radiating heat

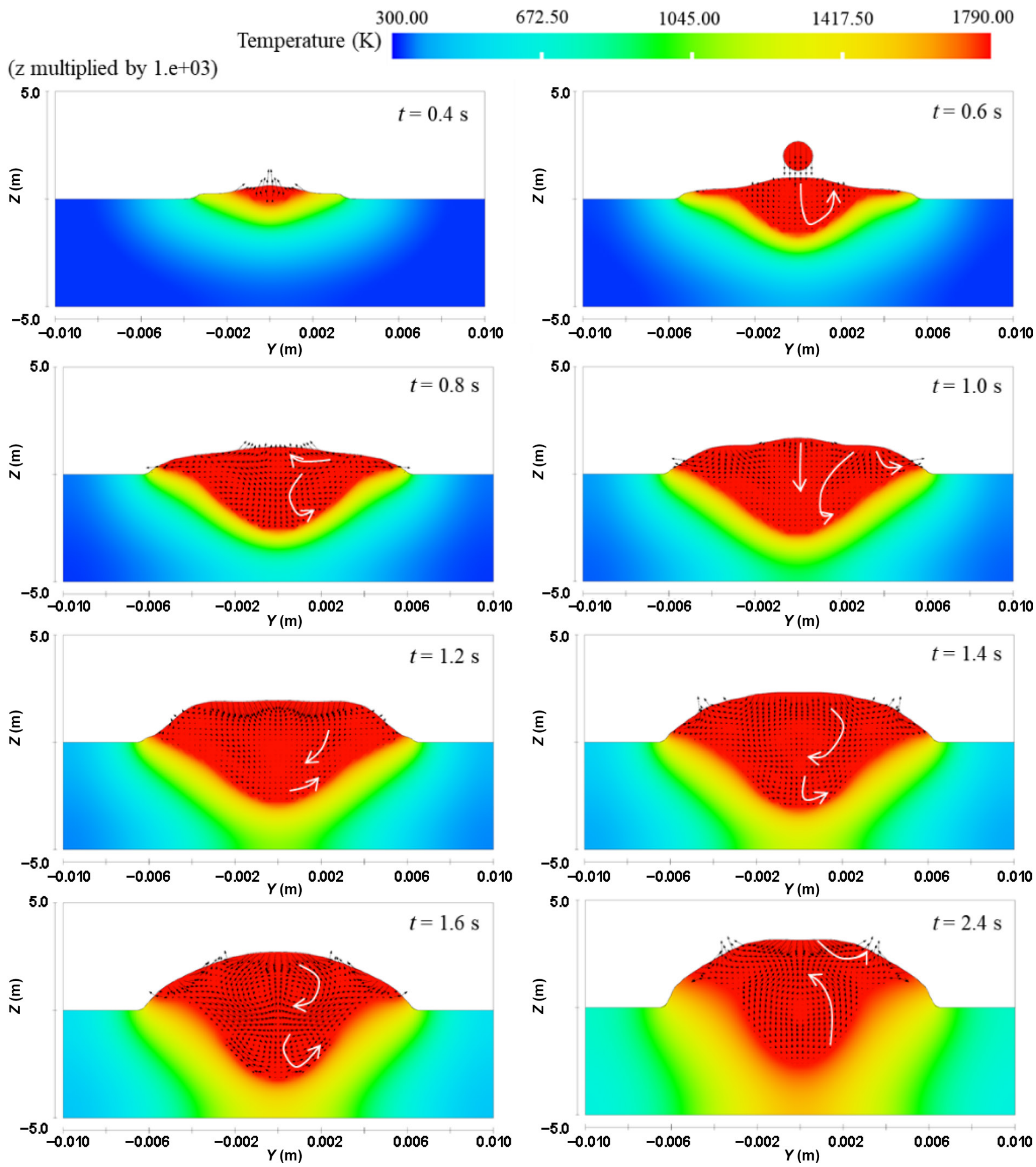

Fig. 9 Temperature and velocity field distributions in cross-sectional view of melt pool at various time intervals.

to the pool's edges. This results in an increase in the width of the molten pool, resulting in a shallow and wide shape. As the solidification process continues, the influence of droplet impact and electromagnetic forces diminishes. However, the tendency for downward flow, driven by electromagnetic forces, remains in the region beneath the melt pool, although the flow rate significantly decreases. In contrast, the upward flow becomes more pronounced in this area, driven by buoyancy and surface tension.

4.3 Simulation results of the microstructure in the cross-sectional view

In this study, the thermal history of case 2's *YZ* cross-section (X = 0.005125 m) is incorporated into the ExaCA model to simulate the solidification dynamics of the molten pool influenced by a transient temperature field. The results, as depicted in Fig. 10, illustrate the microstructural evolution during solidification. The

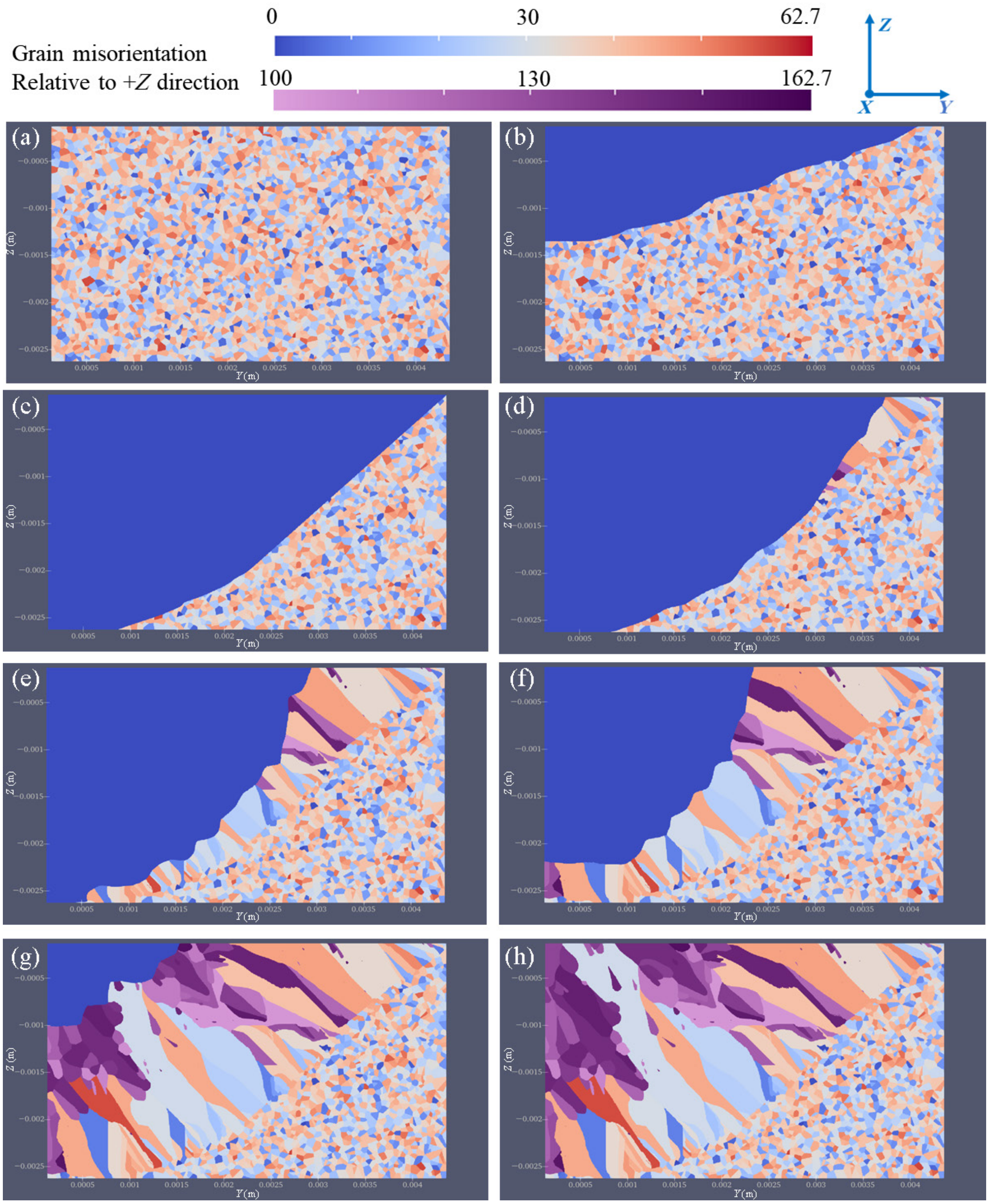

Fig. 10 Microstructural evolution of *YZ* cross-section simulated using ExaCA model.

nucleated grains are represented in pink–purple plots, while epitaxial grains appear in red-blue plots. Specifically, Fig. 10(a) depicts the equiaxed grain microstructure simulated by the model. Figures 10(b) and 10(c) show the initialization of cells undergoing melting-solidification, which transition to the liquid state (blue) in response to macroscopic thermal inputs during the melting phase.

Grain growth in the deposition layer primarily depends on epitaxial crystallization at the fusion line and subsequent competitive grain growth processes. As shown in Fig. 10(d), during the early stages of solidification, the temperature gradient near the fusion line is high, and the constitutional undercooling region is narrow. These conditions promote the nucleation and directional growth of columnar grains, which propagate along the normal direction of the fusion line. During the continuous growth of grains along the preferential growth direction (the direction with the fastest temperature drop) [32], there is an intense competitive growth phenomenon (Figs. 10(e) and 10(f)) due to the decreasing growth space.

As solidification progresses, the temperature gradient within the deposition layer decreases, while constitutional undercooling increases, reducing the grain growth rate and promoting nucleation. As depicted in Figs. 10(g) and 10(h), newly nucleated grains begin to obstruct the growth of initial columnar grains, resulting in the formation of finer equiaxed grains. Similar observations have been reported for the additive manufacturing of Ti–6Al–4V, where columnar grain formation and epitaxial development are prevalent. Radial columnar grain distributions, aligned with heat flux, are commonly observed in cross-sections perpendicular to the heat source scan direction during single-track processing, as demonstrated in selective electron beam melting of Ti–6Al–4V microstructures under varying processing conditions [40,41]. This columnar structure arises from steep thermal gradients within the melt pool, with the base plate and solidified material serving as heat sinks, while surrounding loose titanium powder provides thermal insulation. These conditions enable rapid columnar grain growth along the thermal gradient, with limited nucleation ahead of the solidification front, resulting in epitaxial regrowth across successive melted layers.

Figure 11 displays the simulated *YZ* cross-section, represented by an inverse pole figure (IPF) map generated in MTEX [42] relative to the *Z* direction. The substrate region exhibits a relatively uniform crystal structure, characterized by random grain orientation and weak texture, with no distinct preferential alignment. Within the melt pool, the grain size varies, yet a consistent growth direction is evident in the columnar crystal region. This alignment results from the uniform heat dissipation direction within this area during the deposition process.

Figure 12 presents the pole figure map of the simulated *YZ* cross-section, revealing a pronounced texture strength at the (100) plane, which is the result of solidification along the direction of the maximum thermal gradient. The orientation density functions (ODFs) derived from EBSD data can be compared with those estimated from pole figure data using the calcerror command in MTEX [42]. Additionally, the simulated EBSD function in MTEX allows the simulation of EBSD data based on a given ODF. One of MTEX's key functionalities, calcODF, estimates ODF from pole figure or EBSD data using an advanced method that discretizes

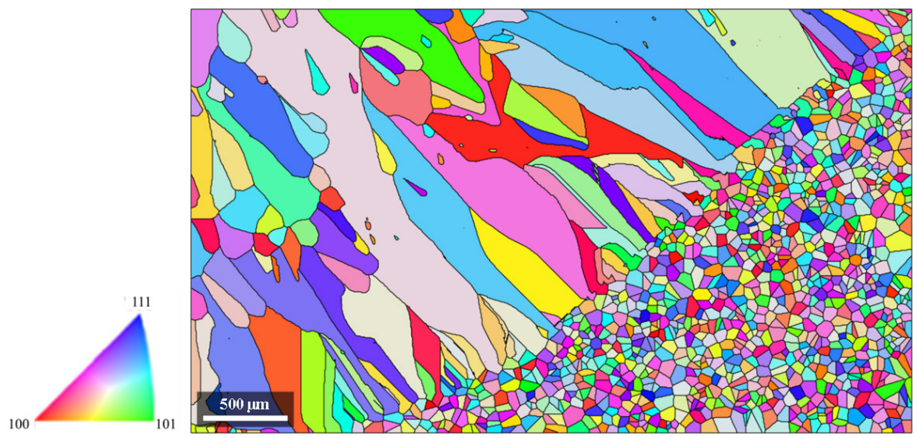

Fig. 11 Simulated microstructure of *YZ* cross-section from ExaCA simulation.

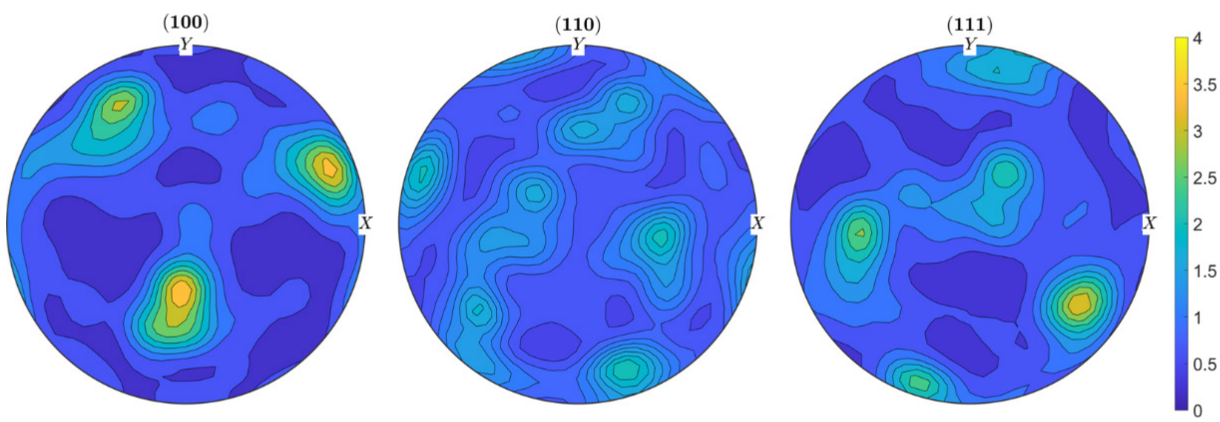

Fig. 12 Pole figure textures from corresponding ExaCA-simulated *YZ* cross-section.

the orientation density space with unimodal radially symmetric functions and employs their fast spherical Fourier transform for efficient computation.

5 Conclusions

In this study, single-layer single-pass deposition of 921A steel was performed using WM960S wire as the feedstock and an arc as the heat source to enable rapid additive manufacturing. The microstructural morphology and dimensional characteristics of the deposition layer were examined at various deposition speeds. Additionally, the macroscopic temperature and flow fields, along with the melt pool cross-sectional microstructure, were simulated. The study yielded the following key conclusions:

(1) Macroscopic metallography of the deposition layer revealed distinct columnar grains aligned with the heat flow direction, accompanied by acicular ferrite and small amounts of granular bainite.

(2) As the deposition speed increased, both the width and height of the deposition layer decreased. The simulated and experimental results for the forming dimensions were in good agreement. At higher deposition speeds, the flow capability of the molten pool was reduced.

(3) In the center of the melt pool, metal flows primarily downward because of the combined effects of electromagnetic force, gravity, and the impact force from molten droplets. At the edges of the melt pool, metal undergoes reflux at the pool's base, where surface tension predominates.

(4) The ExaCA model simulated the growth of columnar grains along the normal direction of the fusion line in the *YZ* cross-section, with nucleated equiaxed grains forming in the center of the melt pool, thereby obstructing the growth of original columnar grains.

Acknowledgements

The authors would like to acknowledge the financial support from the National Key R&D Program of China (No. 2022YFB4600902), the National Natural Science Foundation of China (Nos. 52275349 and 52035005), the Shandong Provincial Science Foundation for Outstanding Young Scholars (No. ZR2024YQ020), the Excellent Young Team Project of Central Universities (No. 2023QNTD002), and the Key R&D Program of Shandong Province (No. 2021ZLGX01).

Author contributions

Lei Shi: Investigation, conceptualization, methodology, data curation, formal analysis, project administration, funding acquisition, supervision, resources, and writing-original draft. Xianhui Lyu: Investigation, data curation, formal analysis, visualization, and writing-review & editing. Ji Chen: Validation, formal analysis, resource, funding acquisition, and writing-review & editing. Chuansong Wu: Validation, formal analysis, resource, funding acquisition, and writing-review & editing. Ashish Kumar: Validation, formal analysis, and writing-review & editing. Ming Zhai: Validation, formal analysis, and writing-review & editing. Wenjian Ren: Validation, formal analysis, and writing-review & editing.

Availability of data and materials

Not applicable.

Competing interests

The authors have no competing interests to declare that are relevant to the content of this article.

References

[1] Yi H, Jia L, Ding JL, *et al.* Achieving material diversity in wire arc additive manufacturing: Leaping from alloys to composites *via* wire innovation. *Int J Mach Tools Manuf* 2024, **194**: 104103.

[2] Bayat M, Zinovieva O, Ferrari F, *et al.* Holistic computational design within additive manufacturing through topology optimization combined with multiphysics multi-scale materials and process modelling. *Prog Mater Sci* 2023, **138**: 101129.

[3] Zhang XT, Wang L, Zhao N, *et al.* The effect of thermal cycle on microstructure evolution and mechanical properties of Co-free maraging steel produced by wire arc additive manufacturing. *J Mater Process Technol* 2024, **332**: 118582.

[4] Li C, Duan CH, Qi YC, *et al.* Effect of shielding gas on MIG welding performance with austenitic wire. *Mater Lett* 2023, **339**: 134118.

[5] Peng K, Yang CL, Lin SB, *et al.* Thermal cycles and its effect on HAZ microstructure and mechanical properties of 10CrNi3MoV steel in double-sided double arc welding. *Int J Adv Manuf Technol* 2017, **93**: 967–974.

[6] Tian G, Wang XM, Wang WY, *et al.* Microstructure, mechanical properties, and galvanic corrosion of 10CrNi3MoV fabricated by wire arc additive manufacturing. *Metals* 2021, **11**: 1235.

[7] Ou W, Mukherjee T, Knapp GL, *et al.* Fusion zone geometries, cooling rates and solidification parameters during wire arc additive manufacturing. *Int J Heat Mass Tran* 2018, **127**: 1084–1094.

[8] Cadiou S, Courtois M, Carin M, *et al.* 3D heat transfer, fluid flow and electromagnetic model for cold metal transfer wire arc additive manufacturing (Cmt-Waam). *Addit Manuf* 2020, **36**: 101541.

[9] Ji FL, Qin XP, Hu ZQ, *et al.* Influence of ultrasonic vibration on molten pool behavior and deposition layer forming morphology for wire and arc additive manufacturing. *Int Commun Heat Mass* 2022, **130**: 105789.

[10] Rodrigues TA, Duarte V, Avila JA, *et al.* Wire and arc additive manufacturing of HSLA steel: Effect of thermal cycles on microstructure and mechanical properties. *Addit Manuf* 2019, **27**: 440–450.

[11] Meier C, Penny RW, Zou Y, *et al.* Thermophysical phenomena in metal additive manufacturing by selective laser melting: Fundamentals, modeling, simulation and experimentation. In: *Annual Review of Heat Transfer*, Zhang ZM, Prasad V, Jaluria Y, Eds. Danbury (USA): Begell House Inc., 2017: 241–316.

[12] Chen JW, Huang CY, Lian YP, *et al.* Numerical simulation on metallic additive manufacturing. *Sci Sin Phys Mech Astron* 2020, **50**: 090007.

[13] Körner C, Markl M, Koepf JA. Modeling and simulation of microstructure evolution for additive manufacturing of metals: A critical review. *Metall Mater Trans A* 2020, **51**: 4970–4983.

[14] Yang Z, Sista S, Elmer JW, *et al.* Three dimensional Monte Carlo simulation of grain growth during GTA welding of titanium. *Acta Mater* 2000, **48**: 4813–4825.

[15] Mishra S, DebRoy T. Measurements and Monte Carlo simulation of grain growth in the heat-affected zone of Ti–6Al–4V welds. *Acta Mater* 2004, **52**: 1183–1192.

[16] Tourret D, Song Y, Clarke AJ, *et al.* Grain growth competition during thin-sample directional solidification of dendritic microstructures: A phase-field study. *Acta Mater* 2017, **122**: 220–235.

[17] Echebarria B, Folch R, Karma A, *et al.* Quantitative phase-field model of alloy solidification. *Phys Rev E* 2004, **70**: 061604.

[18] Rappaz M, Gandin CA. Probabilistic modelling of microstructure formation in solidification processes. *Acta Metall Mater* 1993, **41**: 345–360.

[19] Gandin CA, Rappaz M. A coupled finite element-cellular automaton model for the prediction of dendritic grain structures in solidification processes. *Acta Metall Mater* 1994, **42**: 2233–2246.

[20] Janssens KGF. Random grid, three-dimensional, space-time coupled cellular automata for the simulation of recrystallization and grain growth. *Model Simul Mater Sc* 2003, **11**: 157–171.

[21] Koepf JA, Soldner D, Ramsperger M, *et al*. Numerical microstructure prediction by a coupled finite element cellular automaton model for selective electron beam melting. *Comput Mater Sci* 2019, **162**: 148–155.
[22] Shi RP, Khairallah S, Heo TW, *et al*. Integrated simulation framework for additively manufactured Ti–6Al–4V: Melt pool dynamics, microstructure, solid-state phase transformation, and microelastic response. *JOM* 2019, **71**: 3640–3655.
[23] Zinoviev A, Zinovieva O, Ploshikhin V, *et al*. Evolution of grain structure during laser additive manufacturing. Simulation by a cellular automata method. *Mater Des* 2016, **106**: 321–329.
[24] Gu C, Wei Y, Zhan X, *et al*. A three-dimensional cellular automaton model of dendrite growth with stochastic orientation during the solidification in the molten pool of binary alloy. *Sci Technol Weld Joi* 2017, **22**: 47–58.
[25] Chen SJ, Guillemot G, Gandin CA. Three-dimensional cellular automaton-finite element modeling of solidification grain structures for arc-welding processes. *Acta Mater* 2016, **115**: 448–467.
[26] Xue CD, Blanc N, Soulié F, *et al*. Structure and texture simulations in fusion welding processes–comparison with experimental data. *Materialia* 2022, **21**: 101305.
[27] Koepf JA, Gotterbarm MR, Markl M, *et al*. 3D multi-layer grain structure simulation of powder bed fusion additive manufacturing. *Acta Mater* 2018, **115**: 119–126.
[28] Rolchigo M, Reeve ST, Stump B, *et al*. ExaCA: A performance portable exascale cellular automata application for alloy solidification modeling. *Comput Mater Sci* 2022, **214**: 111692.
[29] Rolchigo M, Carson R, Belak J. Understanding uncertainty in microstructure evolution and constitutive properties in additive process modeling. *Metals* 2022, **12**: 324.
[30] Cho DW, Cho WI, Na SJ. Modeling and simulation of arc: Laser and hybrid welding process. *J Manuf Process* 2014, **16**: 26–55.
[31] Gao ZG, Wu YX, Huang J. Analysis of weld pool dynamic during stationary laser–MIG hybrid welding. *Int J Adv Manuf Technol* 2009, **44**: 870–879.
[32] Li JH, Zhou XL, Brochu M, *et al*. Solidification microstructure simulation of Ti–6Al–4V in metal additive manufacturing: A review. *Addit Manuf* 2020, **31**: 100989.
[33] Liang GD, Qin GL, Cao PZ, *et al*. Numerical investigation of sidewall penetration in narrow gap oscillating laser welding process. *Opt Laser Technol* 2024, **170**: 110282.
[34] Wu DS, Tashiro S, Wu ZA, *et al*. Analysis of heat transfer and material flow in hybrid KPAW–GMAW process based on the novel three dimensional CFD simulation. *Int J Heat Mass Tran* 2020, **147**: 118921.
[35] Song W, Liu XS, Wang P, *et al*. Strength mismatch effect on residual stress of 10CrNi3MoV steel considering the back-chipping process. *Int J Press Vessels Pip* 2022, **195**: 104570.
[36] Rai A, Helmer H, Körner C. Simulation of grain structure evolution during powder bed based additive manufacturing. *Addit Manuf* 2017, **13**: 124–134.
[37] Kurz W, Giovanola B, Trivedi R. Theory of microstructural development during rapid solidification. *Acta Metall* 1986, **34**: 823–830.
[38] Li XX, Tan WD. Numerical investigation of effects of nucleation mechanisms on grain structure in metal additive manufacturing. *Comput Mater Sci* 2018, **153**: 159–169.
[39] Lian YP, Lin S, Yan WT, *et al*. A parallelized three-dimensional cellular automaton model for grain growth during additive manufacturing. *Comput Mech* 2018, **61**: 543–558.
[40] Antonysamy AA, Meyer J, Prangnell PB. Effect of build geometry on the β-grain structure and texture in additive manufacture of Ti–6Al–4V by selective electron beam melting. *Mater Charact* 2013, **84**: 153–168.
[41] Al-Bermani SS, Blackmore ML, Zhang W, *et al*. The origin of microstructural diversity, texture, and mechanical properties in electron beam melted Ti–6Al–4V. *Metall Mater Trans A* 2010, **41**: 3422–3434.
[42] Bachmann F, Hielscher R, Schaeben H. Texture analysis with MTEX–free and open source software toolbox. *Solid State Phenom* 2010, **160**: 63–68.

Lei Shi is currently a professor at the School of Materials Science and Engineering, Shandong University, China. He received his doctoral degree from Shandong University in 2016. His research interests include friction stir welding and additive manufacturing.